

UC San Diego

UC San Diego Previously Published Works

Title

ABCB-mediated shootward auxin transport feeds into the root clock.

Permalink

<https://escholarship.org/uc/item/7dk806pr>

Journal

EMBO Reports, 24(4)

Authors

Chen, Jian

Hu, Yangjie

Hao, Pengchao

et al.

Publication Date













2023-04-05

DOI

10.15252/embr.202256271

Peer reviewed

ABCB-mediated shootward auxin transport feeds into the root clock

Jian Chen^{1,2,†} , Yangjie Hu^{3,†} , Pengchao Hao⁴ , Tashi Tsering⁴, Jian Xia⁴ , Yuqin Zhang³, Ohad Roth³ , Maria F Njo^{1,2} , Lieven Sterck^{1,2} , Yun Hu⁵, Yunde Zhao⁵, Danny Geelen⁶ , Markus Geisler⁴ , Eilon Shani³ , Tom Beekman^{1,2,*}  & Steffen Vanneste^{1,2,6,7,**,†,#} 

Abstract

Although strongly influenced by environmental conditions, lateral root (LR) positioning along the primary root appears to follow obediently an internal spacing mechanism dictated by auxin oscillations that prepattern the primary root, referred to as the root clock. Surprisingly, none of the hitherto characterized PIN- and ABCB-type auxin transporters seem to be involved in this LR pre patterning mechanism. Here, we characterize ABCB15, 16, 17, 18, and 22 (ABCB15-22) as novel auxin-transporting ABCBs. Knock-down and genome editing of this genetically linked group of ABCBs caused strongly reduced LR densities. These phenotypes were correlated with reduced amplitude, but not reduced frequency of the root clock oscillation. High-resolution auxin transport assays and tissue-specific silencing revealed contributions of ABCB15-22 to shootward auxin transport in the lateral root cap (LRC) and epidermis, thereby explaining the reduced auxin oscillation. Jointly, these data support a model in which LRC-derived auxin contributes to the root clock amplitude.

Keywords ABCB; auxin transport; lateral root; root meristem

Subject Categories Membrane & Trafficking; Plant Biology

DOI 10.15252/embr.202256271 | Received 11 October 2022 | Revised 29

November 2022 | Accepted 10 January 2023 | Published online 31 January 2023

EMBO Reports (2023) 24: e56271

Introduction

The root system of plants is of vital importance for their growth and survival as it anchors the plant in the soil and is required for the uptake of water and nutrients and symbiotic interactions. The complexity of root systems can be easily expanded by LR branching

according to environmentally imposed limitations and stimuli (Motte *et al*, 2019). LR development is a multistep process occurring over a long time, involving coordinated signaling across several tissues (Stoeckle *et al*, 2018). The plant hormone auxin is a key regulator of many organogenetic events in plants (Vanneste & Friml, 2009). Its local accumulation triggers dramatic, preprogrammed transcriptional changes that are associated with the progression of the developmental program (Vanneste & Friml, 2009). This is also the case for LR development, where auxin accumulation defines the positioning of prebranch sites (PBS) along the primary root, and thus root architecture complexity (De Smet *et al*, 2007; Dubrovsky *et al*, 2008; Moreno-Risueno *et al*, 2010; Xuan *et al*, 2016). Therefore, plants have established intricate mechanisms to control auxin distribution within tissues (Rosquete *et al*, 2012; Adamowski & Friml, 2015), which can be adjusted according to the developmental stage, hormones, and environmental signals (Motte *et al*, 2019). In the current model, it is proposed that the decision to initiate LR formation is made in a zone close to the meristem (De Smet *et al*, 2007; De Rybel *et al*, 2010). In this zone, oscillatory gene expression, also referred to as the root clock, was reported to correlate with the activity of the auxin signaling output reporter *DR5:LUC* (Moreno-Risueno *et al*, 2010). This periodic auxin signaling selects a subset of cells to gain a higher competence to form a LR reflected in a maintained expression of the auxin output reporter *DR5:LUC*. These sites together with the developing LRs display strong *DR5:LUC* activity and are together referred to as PBS (Moreno-Risueno *et al*, 2010). Indole-3-butyric acid (IBA) to indole-3-acetic acid (IAA) conversion in the LRC contributes to the amplitude of this oscillation (De Rybel *et al*, 2012; Xuan *et al*, 2015), and cyclic programmed cell death of the LRC contributes to the frequency of this oscillation (Xuan *et al*, 2016). An alternative model is the reflux-and-growth model, which proposes auxin oscillations are an emergent feature associated with meristem cell division and

1 Department of Plant Biotechnology and Bioinformatics, Ghent University, Ghent, Belgium

2 Center for Plant Systems Biology, VIB, Ghent, Belgium

3 School of Plant Sciences and Food Security, Tel-Aviv University, Tel-Aviv, Israel

4 Department of Biology, University of Fribourg, Fribourg, Switzerland

5 Section of Cell and Developmental Biology, University of California San Diego, La Jolla, CA, USA

6 Department of Plants and Crops, Ghent University, Ghent, Belgium

7 Lab of Plant Growth Analysis, Ghent University Global Campus, Incheon, Republic of Korea

*Corresponding author. Tel: +32 92646097; E-mail: tobee@psb.vib-ugent.be

**Corresponding author. Tel: +32 93313830; E-mail: steffen.vanneste@ugent.be

†These authors contributed equally to this work as first authors

#Correction added on 5 April 2023, after first online publication: The affiliation footnotes of Steffen Vanneste have been updated.

elongation (van den Berg *et al*, 2021). In this model, cell division and meristem size determine the oscillation frequency, while cell elongation controls oscillation amplitude.

The prevailing model of auxin transport in the root meristem can best be summarized as a reverse fountain of auxin flowing rootward through the vascular tissue and being redirected shootward through the outer layers of the meristem (Grieneisen *et al*, 2007). This outer shootward auxin flow is thought to rejoin the central rootward auxin flow. Both aforementioned LR prepatterning models are based on the principles outlined by the reverse fountain model.

The reverse fountain model for auxin transport is based on cell-to-cell transport via a highly coordinated network of auxin uptake and efflux carriers. The uptake of IAA is mainly affected by efficient IAA⁻/H⁺ symporter via AUX1/Like-AUX1 family members (Swarup & Bhosale, 2019). Multiple members of the PIN and ABCB protein families are known effectors of cellular efflux. All *Arabidopsis* PINs transport IAA into the endoplasmic reticulum or into the apoplast (Adamowski & Friml, 2015), likely via the proline cross-over-based elevator mechanism of deprotonated, cytosolic IAA⁻ that was recently uncovered (Ung *et al*, 2022; Yang *et al*, 2022). In contrast, of 22 full-sized ABCBs (containing two transmembrane domains and two nucleotide-binding domains) (Kang *et al*, 2011), only ABCB1, ABCB19, ABCB4, ABCB21, ABCB6, ABCB20 have been implicated in auxin transport (Geisler *et al*, 2017; Zhang *et al*, 2018; Jenness *et al*, 2022). ABCB14 was shown to transport malate instead of IAA (Lee *et al*, 2008). Recently, a group of closely related ABCBs (ABCB15,16,17,18, and 22) were predicted to also transport IAA, based on the presence of a diagnostic D/E-P motif (Hao *et al*, 2020). Genetic and biochemical studies have indicated a tight interplay between both PINs and ABCBs (Bandyopadhyay *et al*, 2007; Blake-slee *et al*, 2007; Mravec *et al*, 2008; Deslauriers & Spalding, 2021). A recent simulation of auxin transport in the root meristem identified strong PIN-ABCB co-dependent auxin efflux, in combination with individual auxin transport activities, and fluxes via plasmodesmata as the most likely scenario underpinning auxin transport in the root tip (Mellor *et al*, 2020, 2022). The proposed auxin transport components of the reverse fountain are AUX1, for auxin uptake, in combination with PIN1, PIN2, PIN3, PIN4, PIN7, ABCB1, ABCB19, and ABCB4 for auxin efflux. Of these key auxin transporters, only AUX1 was experimentally proven to be involved in the auxin component of the root clock (Xuan *et al*, 2016). Despite the strong overlap between the expression domains of PIN2, ABCB1, ABCB4, and ABCB19 efflux carriers, neither the *pin2* mutant, nor the *pin2abcbl1abcb19* triple mutant showed reduced LR densities (Xuan *et al*, 2016). Moreover, the reported *abcb4* root phenotypes seem to be dependent on the growth conditions (Santelia *et al*, 2005; Terasaka *et al*, 2005; Lewis *et al*, 2007; Kubeš *et al*, 2012). This suggests that the auxin efflux component of the root clock is distinct from the currently characterized set of auxin transporters.

Here, we show that five closely related plasma membrane localized ABCBs (ABCB15, 16, 17, 18, and 22) contribute to shootward auxin transport in the root. By characterization of knock-outs and knock-down lines, we found that their reduced LR density correlates with a reduced amplitude of the root clock oscillation. Interestingly, a detailed analysis of the root meristem and LRC of our knock-down lines revealed a strong correlation between LRC cell death rate and root clock oscillation frequency, instead of the predicted reduced oscillation frequency. Jointly, our data expand the repertoire of

auxin-transporting ABCBs to improve our understanding of auxin transport mechanisms in the root.

Results

Loss of function of cluster ABCB15-22 genes causes defects in root system architecture

Of 22 full-sized ABCBs in *Arabidopsis* (Kang *et al*, 2011), we selected five closely related, but poorly characterized ABCBs, ABCB15, 16, 17, 18, and 22 (hereafter ABCB15-22), for detailed functional characterization.

First, we analyzed the phenotype of T-DNA insertion mutants in these genes. None of these single mutants displayed significant defects in LR density (Appendix Fig S1A–E), indicating functional redundancy among these ABCBs. Their proximity on the chromosome precluded generating higher-order mutants by crossing. Therefore, we attempted to simultaneously target multiple members of this subgroup on via CRISPR/Cas9-mediated genome editing and via a silencing approach.

On the one hand, we designed three multiplex genome editing constructs to target multiple members of the group III ABCBs (Appendix Fig S2A–D). From transformants expressing the respective constructs, we could isolate: a line with mutations in the entire subgroup, named *penta*^{CRISPR} (Appendix Fig S2A); three lines with different mutant alleles in *ABCB16*, *17*, *18*, and *22*, named *quadri*^{CRISPR} (lines F33#1, F33#6 and B64) (Appendix Fig S2C and D); and a double mutant in *ABCB16* and *18*, named *b16b18*^{CRISPR} (Appendix Fig S2B). An attempt to delete the entire genomic region via genome-editing was not successful.

On the other hand, we identified within a collection of artificial microRNA (amiRNA) lines (Zhang *et al*, 2018) a homozygous line for *pro35S:amiR-2572* (named *amiR-2572*), overexpressing an amiRNA that is predicted to target *ABCB15*, *ABCB16*, *ABCB17*, *ABCB18*, and *ABCB22* (Appendix Fig S3A and Dataset EV1). Via Q-RT-PCR on dissected root meristems, we confirmed the transcriptional silencing of *ABCB15*, *ABCB16*, *ABCB18*, and *ABCB22* (Appendix Fig S3B). Similarly, by crossing *amiR-2572* to the corresponding YFP-ABCB reporters, we observed reduced protein levels of most of these ABCBs, but not of the non-target *ABCB1* and *ABCB19* (Appendix Fig S3C and D).

Assuming limited overlap of potential off-targets in these independent knock-out and silencing lines, we determined the developmental importance of these genes. Strikingly, the *amiR-2572* line, the *penta*^{CRISPR} and the three *quadri*^{CRISPR} lines all had shorter roots, a reduced LR density (Fig 1A–G) and smaller rosettes in the soil (Appendix Fig S2E and F). Consistently with more genes being mutated, the *penta*^{CRISPR} phenotypes were more outspoken than *quadri*^{CRISPR} and *amiR-2572*, and even showed reduced fertility (Appendix Fig S2E). In contrast, the *b16b18*^{CRISPR} double mutant did not display significant root phenotypes compared to WT (Fig 1A–D). The gradient of phenotypic penetrance in *penta*^{CRISPR} compared to *quadri*^{CRISPR} and *b16b18*^{CRISPR} supports functional redundancy and/or cooperativity among *ABCB15*, *16*, *17*, *18*, and *22*, in the root and shoot.

Together, these analyses suggest a role for members of the ABCB15-22 cluster in root architecture. Additional mutant combinations will be needed to fully dissect the individual contributions of each ABCB to the observed phenotypes.

ABC15-22 control auxin oscillation amplitude

Given the pronounced phenotypes in the root, we focused on understanding the LR defects in these lines. More detailed phenotyping

revealed that *amiR-2572* had a strong reduction in the early LRP stages, without accumulating intermediate LRP stages (Appendix Fig S4A and B), suggesting that the reduced density of emerged LRs in these lines is due to a defect at the level of LR initiation.

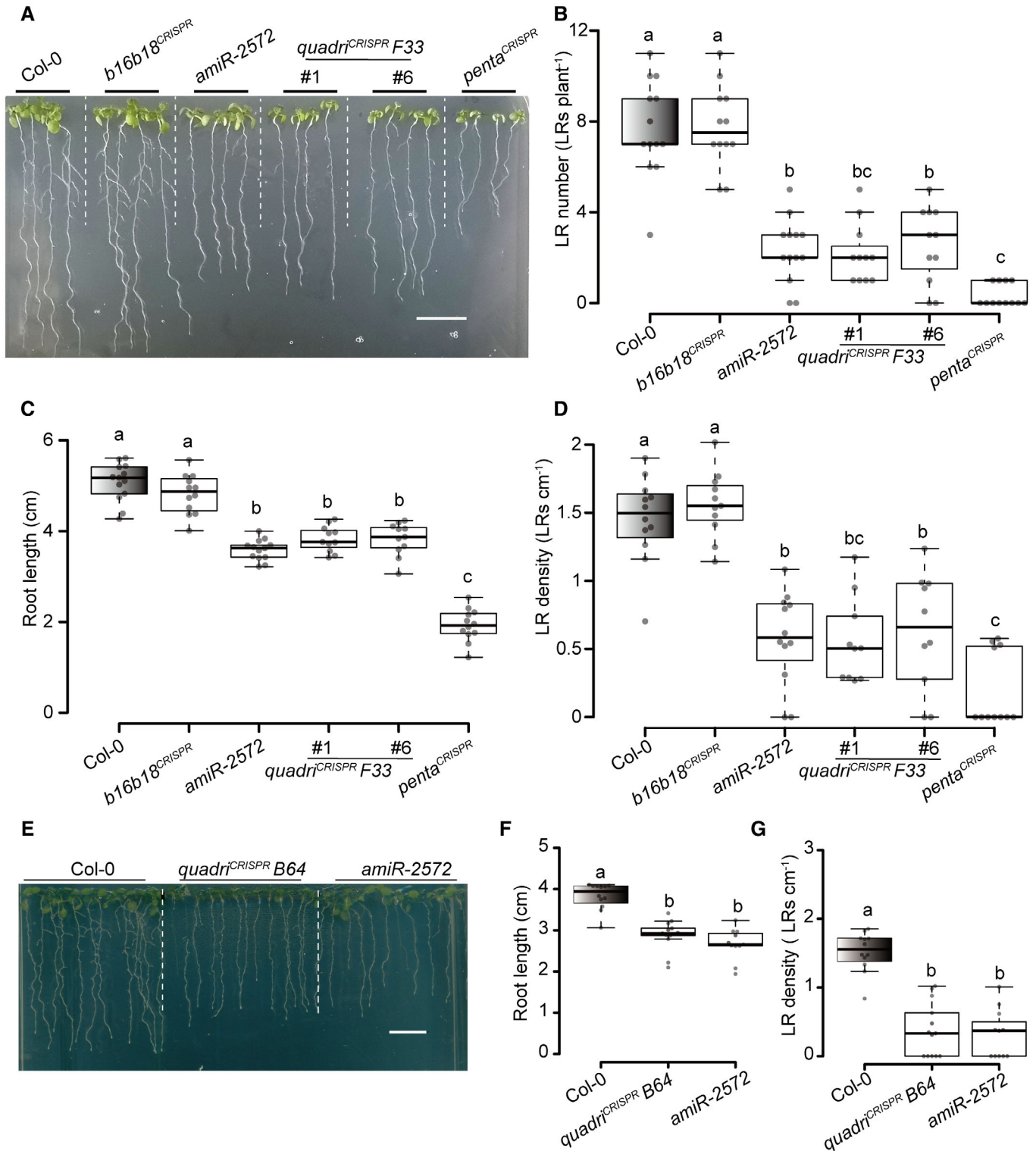


Figure 1.

Figure 1. Silencing and mutating ABCB15-22 causes root architecture defects.

A Macroscopic seedling phenotype of 12-day-old *b16b18^{CRISPR}*, *quadri^{CRISPR} F33#1/#6*, *penta^{CRISPR}* and *amiR-2572*, compared to WT (Col-0). Scale bars = 1 cm.

B–D Boxplots showing the quantification of lateral root number per seedling (B), primary root length (C), and lateral root density (D) in seedlings depicted in (A). $n = 13$ (Col-0), 12 (*b16b18^{CRISPR}*), 13 (*amiR-2572*), 11 (*quadri^{CRISPR} F33#1*), 11 (*quadri^{CRISPR} F33#6*), 12 (*penta^{CRISPR}*).

E Macroscopic seedling phenotype of 12-day-old *quadri^{CRISPR} B64* compared to WT (Col-0) and *amiR-2572*. Scale bars = 1 cm.

F, G Boxplots showing the quantification of primary root length (F) and LR density (G) in seedlings depicted in (E). $n = 12$ (Col-0), 13 (*quadri^{CRISPR} B64*), 11 (*amiR-2572*).

Data information: For (B–D, F, G), One-way ANOVA in combination with Tukey's multiple comparisons test, significant differences ($P \leq 0.05$) are indicated by different lowercase letters. Central bands in the box plots show the medians; box limits indicate the 25th and 75th percentiles as determined by R software; whiskers extend 1.5 times the interquartile range from the 25th and 75th percentiles, outliers are represented by dots.

Source data are available online for this figure.

Lateral root initiation (stage I) is the first anatomical hallmark of LR formation and is preceded by a local maximum of auxin signaling that was installed by the root clock pre-patterning. Such persistent auxin maxima, together with LRP visualized by *DR5:LUC*, hotspots are jointly referred to as prebranch sites (PBS) (Bustillo-Avendano *et al*, 2022) (Appendix Fig S4C). Consistently with the reduced LR initiation (Appendix Fig S4A and B), *amiR-2572* showed a reduced prebranch site density (Fig 2A and B). Prebranch site formation is instructed by an oscillating auxin signaling (*DR5:LUC*) maximum (Appendix Fig S4D–F), of which the oscillation period correlates with the rate of programmed cell death in the LRC, and its amplitude is correlated with the concomitant auxin burst derived from the dying cells (Xuan *et al*, 2016). The root meristem was significantly shorter in *amiR-2572* than in WT (Fig 2C and D). Interestingly, the LRC contained similar numbers of cells in both backgrounds (Fig 2E), with the most distal cell being shorter in *amiR-2572* than in WT (Fig 2F), jointly indicating a reduced cell elongation in the LRC to match the reduced root meristem size. The period of the disappearance of *DR5:VENUS* stripes demarcating cell death in the LRC was also unaffected (Fig 2G and H) and did match with a *DR5:LUC* oscillation period that was similar in *amiR-2572* and wild type (Fig 2I). In contrast, the *DR5:LUC* oscillation amplitude in *amiR-2572* was significantly smaller than in the WT (Fig 2J). That *amiR-2572* impacts on the root clock amplitude, but not its frequency, correlates with the observed LR defect. According to the current model, a sufficiently intense auxin response is required to translate auxin oscillations into prebranch sites, and thus represents a plausible explanation for the LR defect in *amiR-2572*. It is however difficult to exclude effects of the overall reduced growth habit of *amiR-2572*.

ABCB15-22 activities increase cellular IAA efflux

ABCB15, 16, 17, 18, and 22 contain the conserved D/E-P motif that was proposed to be diagnostic of their auxin transporting activities (Hao *et al*, 2020). This, together with the defects in auxin-regulated LR development and root clock amplitude, prompted us to test their auxin transport capacities.

We first determined their subcellular localization. The YFP-ABCB signals co-localized with propidium iodide in *Arabidopsis* roots (Fig 3A; Appendix Fig S5A) and were present in Hechtian strands, connecting the retracted cell to the cell wall after plasmolysis (Fig 3B; Appendix Fig S5B). Similarly, these YFP-ABCBs co-localized with the endocytic tracer dye FM4-64 at the plasma membrane in protoplasts prepared from *Agrobacterium*-transformed *N. benthamiana* leaves (Appendix Fig S5C). Jointly, these data show that ABCB15-22 localize to the plasma membrane.

Overexpression of respective YFP-ABCBs increased the IAA export in *N. benthamiana* mesophyll protoplasts at rates comparable to those seen upon overexpression of the best characterized auxin-transporting ABCB1 (Geisler *et al*, 2005) (Fig 3C). The presence of intact IAA in the supernatant after protoplast separation demonstrated that the *N. benthamiana*-expressed ABCBs stimulated the export of intact IAA, and not a catabolic product (Appendix Fig S6A and B). Importantly, the loading of radiolabeled substrates was not indirectly influenced by over-expression of ABCB as exemplified for ABCB17 (Appendix Fig S6C). Mutation of P980 of the conserved D/E-P motif in ABCB17 to glycine entirely reverted IAA export to vector control levels (Fig 3C), strongly suggesting that enhanced IAA export upon over-expression of members of this ABCB subgroup is most likely driven directly by these ABCBs, rather than indirectly by upregulation of or interaction with tobacco-endogenous transporters. In contrast, none of these ABCBs enhanced the export of the diffusion control, benzoic acid (BA) (Appendix Fig S6D). Moreover, overexpression of ABCB17, as a representative of this group of transporters did not result in significantly altered export of putative ABC transporter substrates other than IAA, including indole-3-butyric acid (IBA) (Ruzicka *et al*, 2010), abscisic acid (ABA) (Kang *et al*, 2015) and *trans*-zeatin (tZ) (Zhang *et al*, 2014), as well as the ABCB14 substrate, malate (Lee *et al*, 2008) and diffusion control, benzoic acid (BA) (Fig 3D). This apparent high selectivity is especially remarkable for IBA, which differentiates from IAA solely by an extension of 2 C-atoms in the acid moiety.

Conversely, endogenous auxin transport activities were significantly reduced in leaf mesophyll protoplasts of *amiR-2572*, but not in *abc* T-DNA insertion mutants (Fig 3E), without altering BA export (Appendix Fig S6E). This indicates that the ABCBs that are targeted by *amiR-2572* contribute to auxin transport in leaf mesophyll cells.

Jointly, these data highlight ABCB15-22 as a group of ABCBs that stimulate auxin transport.

ABCB15-22 contribute to shootward auxin transport

Previously, we inferred from tissue-specific complementation assays, chemical genetics and *in silico* modeling that shootward auxin transport in the LRC is a critical determinant of auxin oscillation amplitude (De Rybel *et al*, 2012; Xuan *et al*, 2015, 2016). The defect in auxin oscillation amplitude in *amiR-2572*, together with the observed IAA transport activities of ABCB15-22 indicates that they could represent the elusive efflux component in this model. To test this hypothesis, we determined shootward auxin transport rates in *amiR-2572* roots.

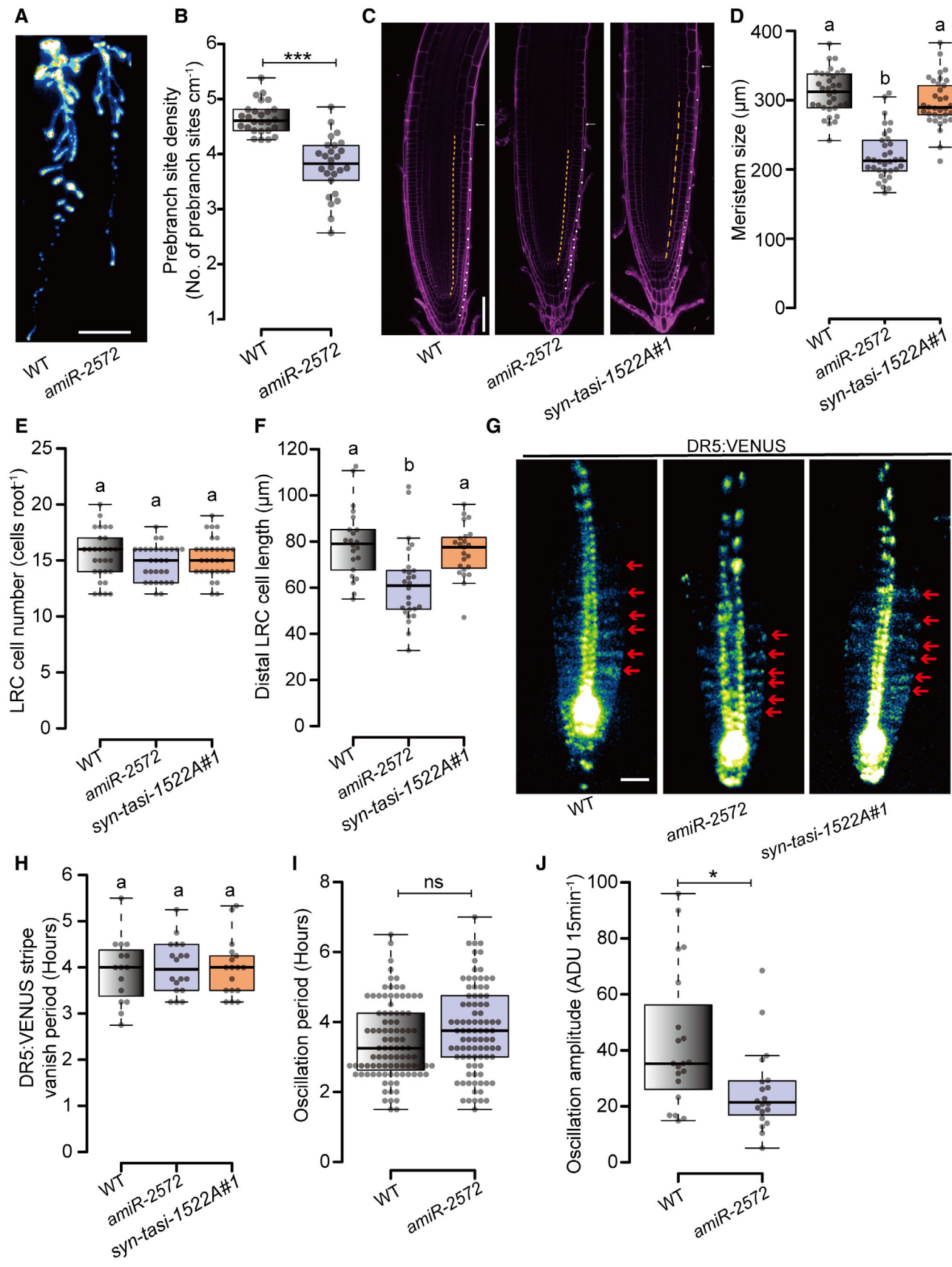


Figure 2.

Figure 2. The *amiR-2572* line has reduced auxin oscillation amplitude and LR density defects.

- A Luciferase image of the whole *WT* and *amiR-2572* seedlings after 10 min exposure to visualize the pre-branch sites in the root by *DR5:LUC* luminescence.
- B Quantification of pre-branch site density in 10-day-old *WT* and *amiR-2572* determined by *DR5:LUC* luminescence, $n = 26$ (*WT* and *amiR-2572*).
- C Confocal images of root tips in 5-day-old *Col-0*, *amiR-2572* and *syn-tasi-1522A#1* seedlings. LRC cells were indicated by white asterisks. The distal LRC cells were indicated by white arrows. The scale bar represents 50 μm .
- D–F Quantification of meristem size (D), LRC cell number (E), and distal LRC cell length (F) in 5-day-old *Col-0*, *amiR-2572* and *syn-tasi-1522A#1* seedlings. The meristem size was measured along the yellow dashed lines in (C), as estimated by the distance from the QC to the first elongating cortical cell, $n_{D/E/F} = 33/30/22$ (*WT*), 34/30/26 (*amiR-2572*) and 37/30/23 (*syn-tasi-1522*) from three independent biological repeats.
- G Macroview stereo microscopic view of *DR5:VENUS* expression in root tips of 3-day-old *WT*, *amiR-2572* and *syn-tasi-1522A#1* seedlings, red arrows indicate *DR5:VENUS* stripes in the lateral root cap. Scale bar = 50 μm .
- H Quantifications of the time interval(s) between the consecutive disappearance of *DR5:VENUS* stripes in the most-distal lateral root cap in 3-day-old *WT*, *amiR-2572* and *syn-tasi-1522A#1*. $n = 15$ (*WT*), 18 (*amiR-2572*) and 17 (*syn-tasi-1522A#1*).
- I, J Quantification of the oscillation period (I) and amplitude (J) of *DR5:LUC* in 3-day-old *WT* and *amiR-2572*, $n = 21$ (*WT* and *amiR-2572*).

Data information: For (B, I, J), Unpaired two-tailed Student's *t*-test with Welch's correction, $P < 0.05$ (*), $P < 0.001$ (***). For (D–F, H), One-way ANOVA in combination with Tukey's multiple comparisons test, significant differences ($P \leq 0.05$) are indicated by different lowercase letters. Central bands in the box plots show the medians; box limits indicate the 25th and 75th percentiles as determined by R software; whiskers extend 1.5 times the interquartile range from the 25th and 75th percentiles, outliers are represented by dots.

Source data are available online for this figure.

Indeed, local, exogenous application of radiolabeled IAA to the root tip, revealed a significant reduction in shootward auxin transport in *amiR-2572* roots (Fig 4A). In a complementary approach, we monitored auxin dynamics in the meristem with cellular resolution, using a recently developed estradiol-inducible auxin biosynthesis system that can be activated specifically in the quiescence center (QC) (*pWOX5:XVE>>YUC1-2A-TAA1*) (Hu et al, 2021). Simultaneous expression of *YUC1* and *TAA1* results in IAA synthesis from tryptophan (Mashiguchi et al, 2011; Won et al, 2011). In *WT* (*Col-0*), estradiol treatment (5 μM) induced a strong ectopic *DR5:VENUS* expression in the LRC, epidermis and the stele in the elongation zone within 7.5 h. These effects were further enhanced after 9 h estradiol treatment (Fig 4B and C). This is consistent with auxin, which was produced in the QC, being transported via the LRC and epidermis towards the tissues of the elongation zone, where it activates *DR5:VENUS* expression. In estradiol-treated *pWOX5:XVE>>YUC1-2A-TAA1 x amiR-2572*, the induction of *DR5:VENUS* in the elongation zone was at both time-points severely reduced compared to the *pWOX5:XVE>>YUC1-2A-TAA1* control (Fig 4B and C). Additionally, we noted a delay in the emergence of lateral roots in induced *pWOX5:XVE>>YUC1-2A-TAA1 x amiR-2572* (Fig 4D), which is consistent with a role in the shootward auxin transport mechanism that contributes to LR formation.

A network of ABCB15-22 expression in the outer tissues of the root

Using *promoter:NLS-GUS-GFP* reporters, we found strong promoter activities for *ABCB15*, *B16*, *B17*, and *B22* in the outer tissues of the root meristem (Fig 5A–C; Appendix Fig S7A–C) and for *ABCB16* in all stages of LR development (Appendix Fig S7B). *ABCB18* was almost not expressed in the root meristem, but showed very weak expression in vascular tissues of the hypocotyl and mature root tissues (Appendix Fig S7C). Confocal microscopy and histological sections revealed that the root meristematic expression of *ABCB15*, *B16*, *B17*, and *B22* was largely restricted to the epidermis and/or LRC (Fig 5A–C). The expression patterns of the ABCB15-22 cluster define a network with overlapping and/or complementary expression across the outer layers of the root, reflecting that they could exert functionally redundant and/or cooperative functions in these tissues.

The expression pattern of the ABCB15-22 members in the outer layers of the root overlaps with those of ABCB4 and the ABCB1/B19 pair, suggesting they could act in the same pathway. Therefore, we crossed *amiR-2572* to *abcb4* and *abcb1abcb19* double mutants. The *amiR-2572* LR and root length phenotypes were epistatic over *abcb4* and *abcb1abcb19* root phenotypes (Appendix Fig S8A–F), suggesting non-overlapping functions within these ABCBs in the regulation of LR density, despite the significant overlap of their expression domains in the root meristem.

Together with the expression patterns and phenotypes, these data are consistent with the ABCB15-22 cluster contributing to shootward auxin transport mechanism in the outer layers of the meristem that contributes to the *DR5:LUC* oscillation amplitude and LR density.

ABCB15-22 activities in the outer layers of the root are involved in PBS formation

The *amiR-2572* line had prominent seedling phenotypes, not only in the shoot, but also had a reduced root meristem size (Fig 2C and D), which complexifies the interpretation of its LR phenotype. To specifically assess the contribution of ABCB15-22 activities in the outer tissues of the root to LR density, we pursued a tissue-specific silencing strategy. Therefore, we used synthetic trans-acting small-interfering RNAs (*syn-tasiRNAs*) in the *AtTAS1c* backbone (Carbonell et al, 2014), that are predicted to target ABCB15, 16, 17, 18, and 22 (*syn-tasi-1522*). Two independent and distinct *syn-tasiRNAs*, indicated as "*syn-tasi-1522A*" and "*syn-tasi-1522B*" (Dataset EV1; Appendix Fig S3A), were expressed in the outer layers of the root (LRC, epidermis, cortex) via the *PIN2* promoter (Marques-Bueno et al, 2016). For both *syn-tasi-1522A* and *syn-tasi-1522B*, we characterized two independent lines. Each line displayed significant reductions in LR density, but not in root length (Appendix Fig S9A–F).

We validated the transcriptional silencing of *ABCB15*, *ABCB16*, *ABCB17*, *ABCB18*, and *ABCB22* via Q-RT-PCR in the strongest line, *syn-tasi-1522A#1* (Appendix Fig S3B). The silencing activities were also confirmed by analyzing the F1 cross to the respective fluorescently labeled ABCB reporters. The crosses with *syn-tasi-1522A#1* revealed significant reductions of YFP-ABCB15, B16, B17, B18, and B22, but not of the more distantly related ABCB1-GFP or ABCB19-

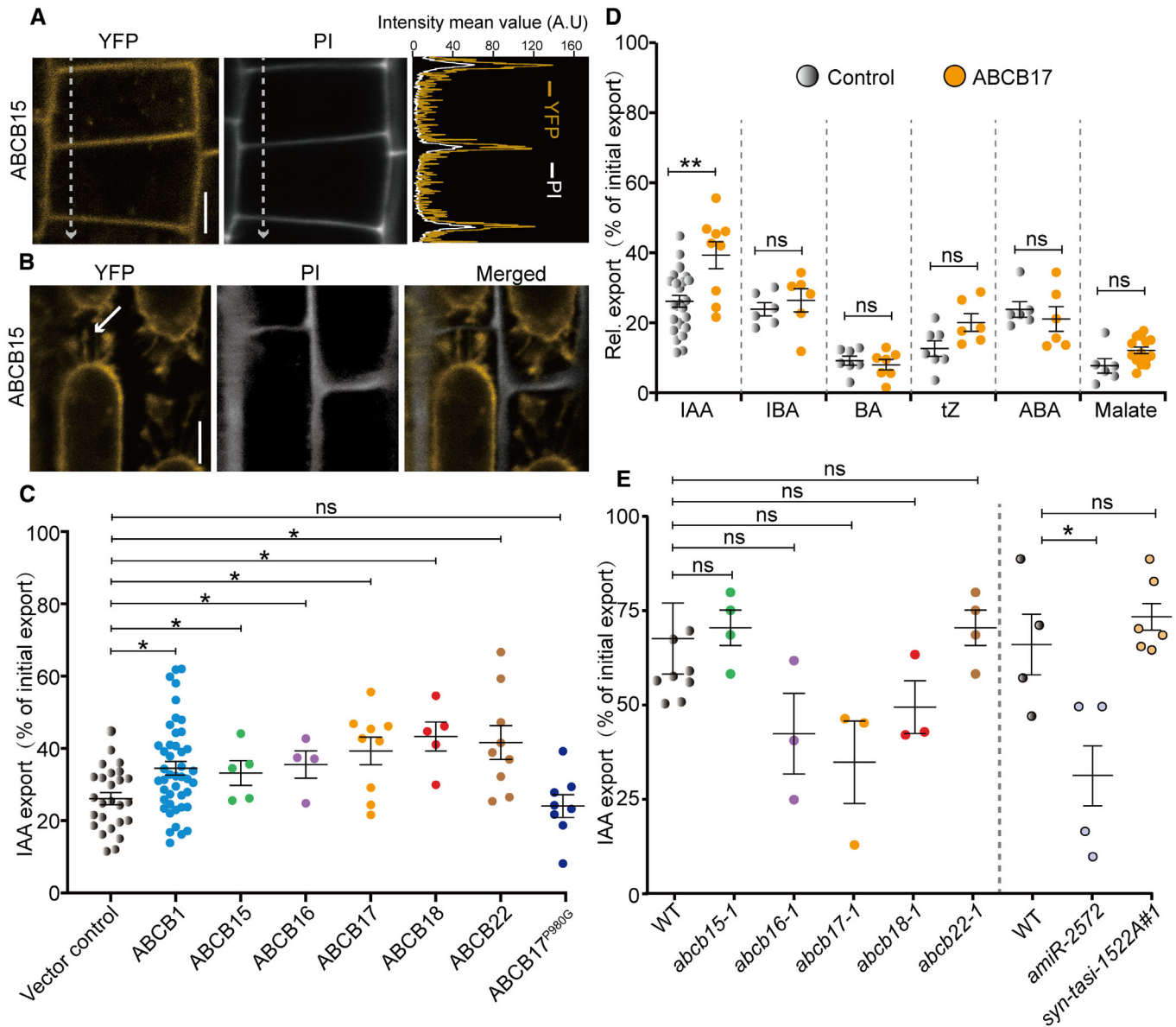


Figure 3. Analysis of plasma membrane localization and cellular transport activities.

A Co-localization of YFP-ABC15 with Propidium Iodide (PI) in root epidermal cells of 3-day-old seedlings. A plot of the fluorescence intensity of YFP and PI along the dashed lines shows the colocalization of the YFP and PI intensity peaks. Scale bars = 10 μ m.

B Presence of YFP-ABC15 on Hechtian strands of epidermal cells of 3-day-old seedlings after 10 min 0.8 M mannitol treatment. Cell walls are counterstained by Propidium Iodide (PI). The white arrow indicated the Hechtian strands. Scale bars = 10 μ m.

C IAA export assay. Export of [3 H]-IAA, assayed in parallel from tobacco mesophyll protoplasts expressing ABCB1, ABCB15-22 and ABCB17^{P980C} against vector control. mean \pm SE; n = 26 (vector control), 44 (ABCB1), 5 (ABCB15), 4 (ABCB16), 9 (ABCB17), 5 (ABCB18), 9 (ABCB22) and 8 (ABCB17^{P980C}), transport experiments generated from independent tobacco transfections.

D Export assay of plant hormones IAA ($n_{VC/ABCB17}$ = 26/9), IBA ($n_{VC/ABCB17}$ = 6/6), BA ($n_{VC/ABCB17}$ = 7/7), ABA ($n_{VC/ABCB17}$ = 6/6), tZ ($n_{VC/ABCB17}$ = 7/6) and malate ($n_{VC/ABCB17}$ = 6/16) in parallel from *N. benthamiana* mesophyll protoplasts expressing ABCB17 against vector control. mean \pm SE; transport experiments generated from independent tobacco transfections.

E [3 H]-IAA export from WT, *abcb15-1*, *abcb16-1*, *abcb17-1*, *abcb18-1*, *abcb22-1*, *amiR-2572* and *syn-tasi-1522A#1* *Arabidopsis* leaf mesophyll protoplasts, mean \pm SE; n = 9 (WT), 4 (*abcb15-1*), 3 (*abcb16-1*, *abcb17-1*, *abcb18-1*) and 4 (*abcb22-1*), n = 4 (WT, *amiR-2572*) and 6 (*syn-tasi-1522A#1*).

Data information: For (C–E), Unpaired two-tailed Student's *t*-test with Welch's correction, P < 0.05 (*), P < 0.01 (**). Source data are available online for this figure.

GFP (Appendix Fig S3C and D). Jointly, these data show efficient and specific silencing of the intended target ABCBs in the *syn-tasi-1522A#1*. Using the same F1 cross strategy, we also assessed the

tissue-specificity of these silencing constructs. The *pro35S*-driven *amiR-2572* caused ubiquitous silencing in the root and the leaf epidermis. In contrast, the *proPIN2*-driven *syn-tasi-1522A#1*

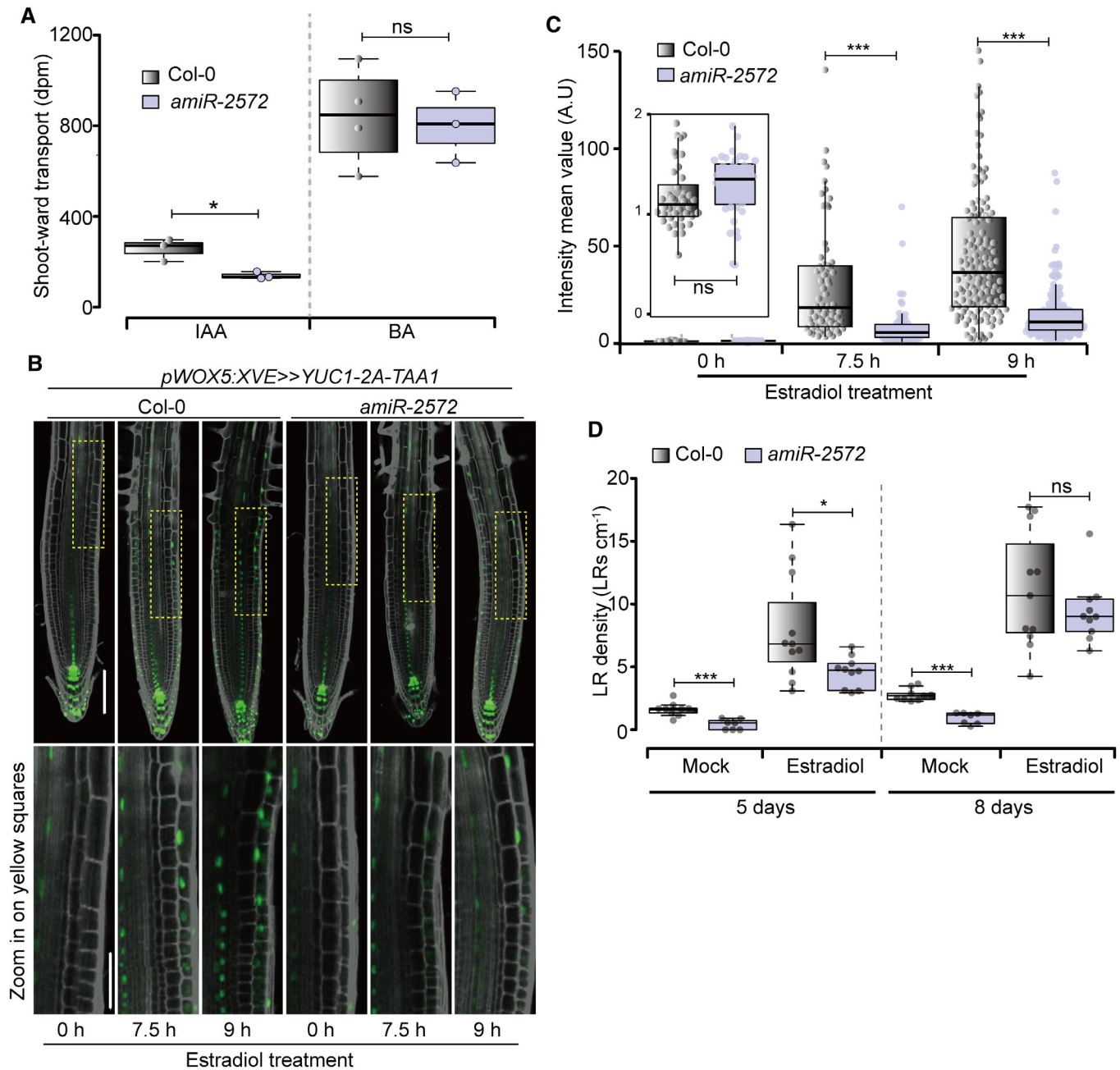


Figure 4. ABCB15-22 contribute to shootward auxin transport for LR induction.

- A** Shootward auxin transport assay of [³H]-IAA and [¹⁴C]-BA in WT (Col-0) and *amiR-2572* roots, mean ± SE; *n* = 3 (Col-0 and *amiR-2572*; IAA); *n* = 4 (Col-0; BA) and 3 (*amiR-2572*; BA).
- B** Analysis of *DR5:VENUS* expression in the root elongation zone of 4-day-old *pWOX5:XVE>>YUC1-2A-TAA1*, in Control and *amiR-2572* treated with β-estradiol (5 μM) for 0, 7.5 and 9 h. Images are composed of several tiles generated in a single snap with automatic assembly, PI in gray. The zoomed images of the yellow squares are presented below each root showing the accumulation of the *DR5:VENUS* signal in the elongation zone. Scale bar = 100 μm.
- C** Quantification of *DR5:VENUS* signals in the epidermis of the elongation zone shown in (B). *n*_{0h} = 40/40, *n*_{7.5h} = 70/70, *n*_{9h} = 140/160 (WT/*amiR-2572*) from at least 4 (0 h), 7 (7.5 h), 14 (9 h) seedlings of each treatment.
- D** LR density of *pWOX5:XVE>>YUC1-2A-TAA1*, in control and *amiR-2572* treated with β-estradiol. Seven-day-old seedlings were transferred to MS plates containing 500 nM β-estradiol. The primary root length and the total number of emerged LRs were recorded after 5 and 8 days of treatment. *n* = 9 (Col-0; Mock), 7 (*amiR-2572*; Mock), 11 (Col-0; Estradiol) and 10 (*amiR-2572*; Estradiol).

Data information: For (A, C, D), Unpaired two-tailed Student's *t*-test with Welch's correction, *P* < 0.05 (*), *P* < 0.001 (***). Central bands in the box plots show the medians; box limits indicate the 25th and 75th percentiles as determined by R software; whiskers extend 1.5 times the interquartile range from the 25th and 75th percentiles, outliers are represented by dots.

Source data are available online for this figure.

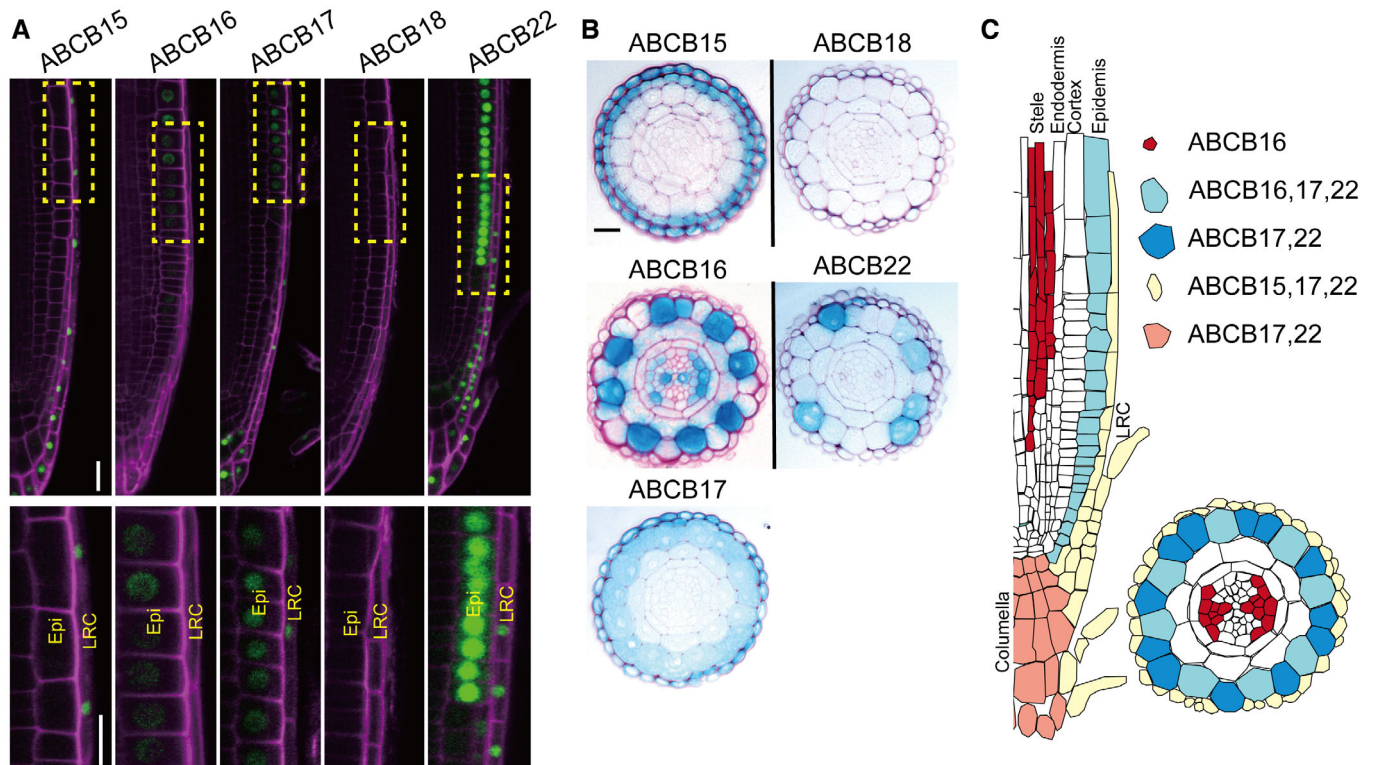


Figure 5. ABCB15-22 expressed in the outer layers of the root meristem.

- A, B Expression pattern of *proABCB15:NLS-GFP-GUS*, *proABCB16:NLS-GFP-GUS*, *proABCB17:NLS-GFP-GUS*, *proABCB18:NLS-GFP-GUS*, and *proABCB22:NLS-GFP-GUS* expression in roots of 3-day-old seedlings, using confocal microscopy showing longitudinal overview pictures (Propidium iodide in magenta), and images zoomed on the epidermis and LRC corresponding to yellow squares (A); cytological sections of GUS stained roots of 3-day-old seedlings, counterstained with ruthenium red (B). Scale bars represent 20 μm for both graphs.
- C Root annotation schematic representation of the summary expression pattern of ABCB15-22 in the root meristem.

silencing activity was largely restricted to the outer layers of the root and was more efficient in these outer root meristem tissues than in *amiR-2572* (Fig 6A–D; Appendix Fig S10). The absence of silencing in the leaf of *syn-tasi-1522A#1*, in comparison to *amiR-2572* (Fig 6A and E), matched a lack of auxin transport defects in leaf mesophyll cells (Fig 3E, Appendix Fig S6E). Therefore, *syn-tasi-1522A#1* phenotypes should mainly derive from gene silencing in the outer tissues of the root. The lack of overt root length, meristem or LRC defects in *syn-tasi-1522A#1* (Fig 2C–F) compared to *amiR-2572*, therefore demonstrates that ABCB15-22 have additional roles in overall plant growth and development. Importantly, a significant reduction in LR initiation (Appendix Fig S9G and H), prebranch site formation (Fig 6F), and reduced *DR5:LUC* oscillation amplitude (Fig 6G and H) could still be detected. These data suggest that the network of ABCB15-22 activities in the outer layers of the root modulates prebranch site formation via contributions to auxin oscillation amplitude.

Discussion

For a long time, ABCB1/19 and ABCB4/21 were the only characterized auxin-transporting ABCBs (Geisler et al, 2017). Of the remaining ABCBs, ABCB14 was found to import malate (Lee et al, 2008).

Recently, the repertoire of auxin-transporting ABCB was further expanded with the ABCB6/20 pair (Zhang et al, 2018), raising the question if more ABCBs could be classified as auxin transporters. Among all thus far characterized auxin-transporting ABCBs, a conserved D/E-P motif was identified that was not only essential for auxin transport activities, but was also sufficient to introduce a significant auxin transport capacity to the malate-transporting ABCB14 (Hao et al, 2020). ABCB15, 16, 17, 18, and 22 contained this motif, highlighting them as putative auxin transporters. Indeed, we found that overexpression of these ABCBs increases the auxin efflux from tobacco protoplasts and that this activity depends on the presence of an intact D/E-P motif that is proposed as diagnostic for auxin transporting capacity in ABCBs (Hao et al, 2020). Moreover, the *amiR-2572* displayed defects in shootward auxin transport in the root. To control artifacts related to developmental changes in *amiR-2572*, we used tissue-specific silencing lines. The *syn-tasi-1522A#1* displayed root clock amplitude and PBS defects similar to those observed in *amiR-2572*. Using transient overexpression assays, we found increased IAA export from plant cells, while we did not detect a change in the export of the structurally related IBA, malate or other structurally unrelated molecules, suggesting that this group of five ABCBs have a high IAA specificity compared to the PLEIOTROPIC DRUG RESISTANCE (PDR) subclade of ABCGs. In example ABCG36 has been implicated in the transport of auxin

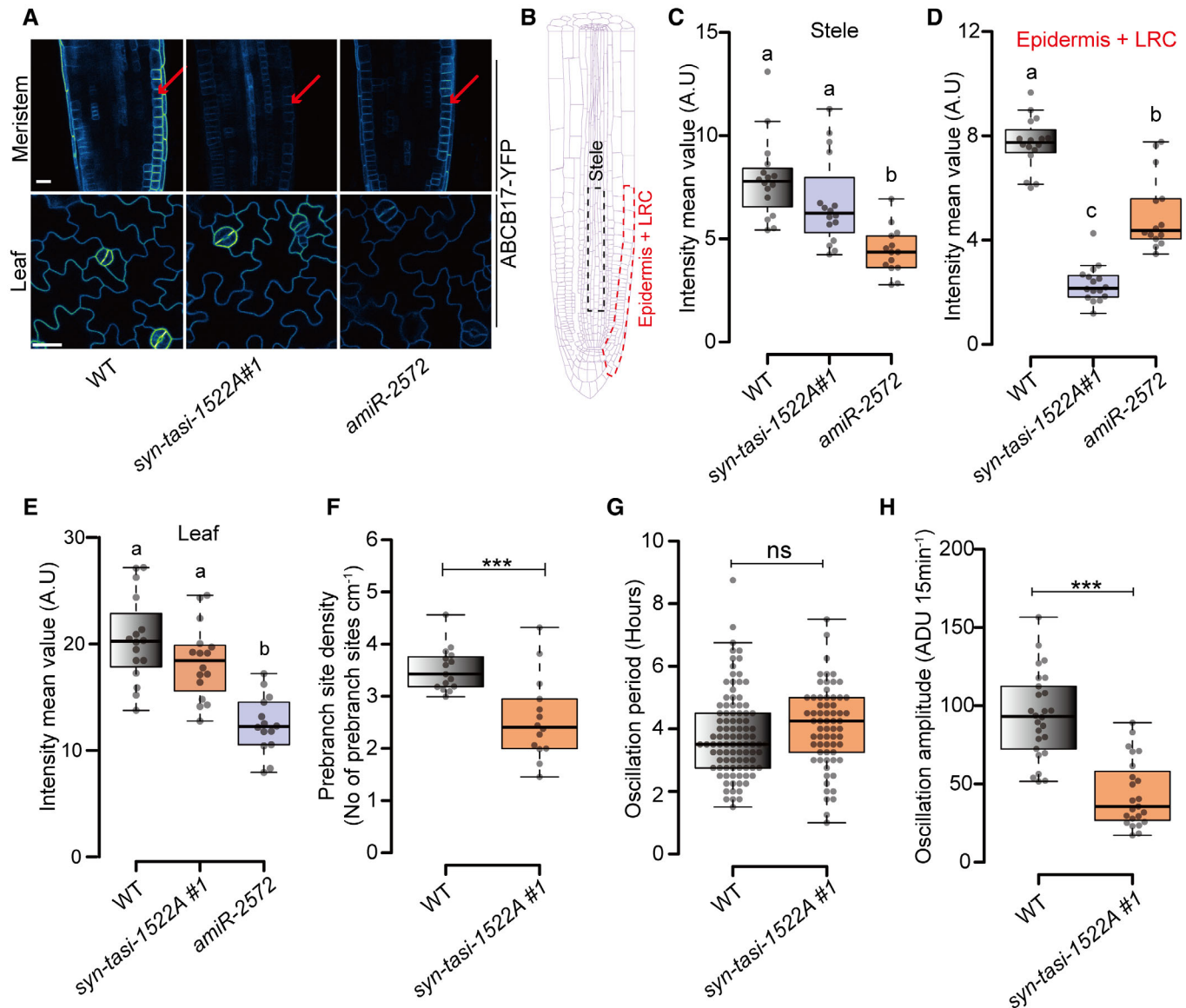


Figure 6. Tissue-specific silencing of ABCB15-22 impairs auxin oscillation amplitude and LR density.

A Fluorescence of YFP-ABCB17 in the root meristem and leaf in 3-day-old F1 crosses with WT, *syn-tasi-1522A#1* and *amiR-2572*, propidium iodide (PI) in magenta. Red arrows highlight the position of the epidermis. Scale bars = 50 μ m.

B Schematic representation of root geometry with the indication of regions of interest for YFP-ABCB17 signal quantification. Red (Stele), and black (epidermis/LRC).

C, D Quantification of YFP-ABCB17 fluorescence intensity in the stele (C) and epidermis/LRC (D) of A, measured at regions of interest corresponding to colors shown in panel (B). $n = 16$ (WT, *syn-tasi-1522A#1*) and 14 (*amiR-2572*).

E Quantification of YFP-ABCB17 fluorescence intensity in the leaf epidermis. The average fluorescence intensity of five cells per leaf was measured as one sample. $n = 16$ (WT, *syn-tasi-1522A#1*) and 14 (*amiR-2572*).

F Quantification of pre-branch site density in 10-day-old WT and *syn-tasi-1522A#1* determined by *DR5::LUC* luminescence, $n = 15$ (WT) and 14 (*syn-tasi-1522A#1*).

G, H Quantification of the oscillation period (G) and amplitude (H) of *DR5::LUC* in 3-day-old WT and *syn-tasi-1522A#1*, $n = 27$ (WT) and 23 (*syn-tasi-1522A#1*).

Data information: For (C–E), One-way ANOVA in combination with Tukey's multiple comparisons tests; significant differences ($P \leq 0.01$) are indicated by different lower-case letters; For (F–H), Unpaired two-tailed Student's *t*-test with Welch's correction, $P < 0.001$ (***). Central bands in the box plots show the medians; box limits indicate the 25th and 75th percentiles as determined by R software; whiskers extend 1.5 times the interquartile range from the 25th and 75th percentiles, outliers are represented by dots.

Source data are available online for this figure.

analogs (2,4-D) and precursors (IBA), auxin transport inhibitor (NPA), but could not transport IAA (Ito & Gray, 2006; Ruzicka et al, 2010). While we cannot exclude that this group of five ABCBs have additional substrates, our data could only detect effects on IAA

transport, suggesting specificity. More work is needed to establish the auxin transport characteristics of these ABCBs, for instance via biochemical assays and heterologous systems. The availability of 11 auxin-transporting ABCBs implies a large potential for functional

redundancy, making it difficult to uncover the contributions of ABCB-mediated auxin transport to developmental processes. This is illustrated by the appearance of increasingly severe phenotypes in double and higher order mutants in *ABCB1*, 4, 6, 19, and 20 (Geisler et al, 2003; Zhang et al, 2018; Jenness et al, 2022). Similarly, we found increasingly penetrant phenotypes with increasing numbers of *ABCB15-22* genes being mutated. While most of them are expressed in the same region, their expression pattern is not fully overlapping, and in some case mainly complementary, resulting in a complex genetic interaction. A full dissection of the genetic interactions among these ABCBs will require additional mutant combinations, tissue-specific complementation, and modeling.

Interestingly, all auxin-transporting ABCBs characterized to date have been shown to be expressed in roots and seem to contribute to auxin transport in the root. Recent models of auxin transport in the root meristem are based only on *ABCB1*, 4 and 19, and could be used to simulate realistic auxin distribution patterns (Mellor et al, 2022). However, the auxin distribution changes predicted by simulating the *abcb4* mutant did not match the experimental findings, a finding that was proposed to be attributable to uncharacterized ABCBs. Our analyses show that *ABCB15-22* are expressed in tissues of the root meristem overlapping with the modeled *ABCB4* activity and seem contribute to shootward auxin transport. Therefore, it will be interesting to evaluate these ABCBs to improve models of auxin transport in the root.

At its core, the spacing of LR in *Arabidopsis* is determined by pre-patterning along the root that is instructed by the periodic activation of auxin signaling in the pericycle (De Smet et al, 2007; Moreno-Risueno et al, 2010; Xuan et al, 2015). This model of LR pre-patterning assumes a local build-up or oscillation of auxin that triggers LR initiation when an auxin signaling threshold is surpassed (Xuan et al, 2015).

Two models based on the reverse fountain auxin transport model have been proposed to explain this oscillation in auxin signaling. In the first model, periodic cell death of the lateral root cap releases auxin into the shootward auxin flow, resulting in a peak of auxin in the stele tissues (Xuan et al, 2016). Consequently, the rate of LRC cell death set the frequency of the oscillation, and the auxin transport rates set the amplitude of the oscillation. In the reflux-and-growth model, cell division and elongation dynamics in a growing root model automatically generate auxin oscillations (van den Berg et al, 2021). In this model, cell division rates and meristem size set the oscillation frequency, while elongation rates determine the priming amplitude. According to the reflux-and-growth model, the smaller meristem in *amiR-2572* should translate into a reduced oscillation frequency and downstream a reduced LR density. Instead, we found that oscillation frequency was unaffected in *amiR-2572* and that this frequency did match with LRC cell death rates. In this background, LRC cell death rates thus seem to have a greater contribution to the auxin oscillation frequency than meristem size and proliferation rates.

Materials and Methods

Plant material and growth conditions

Arabidopsis thaliana Columbia (Col-0) ecotype was used as wild type. *abcb15-1* (SALK_034562) (Kaneda et al, 2011), *abcb16-*

1 (SALK_006491), *abcb17-1* (SALK_002801), *abcb18-1* (SALK_013774), and *abcb22-1* (SALK_202270), *abcb4-2/pgp4-2* (SALK_072038) (Lewis et al, 2007) and *b1-100b19-3(b1b19)* (Wu et al, 2010). *Arabidopsis* transgenic lines *DR5rev:VENUS-N7* (Heisler et al, 2005) and *DR5:LUC* (Moreno-Risueno et al, 2010) were crossed and homozygous lines were selected and used as T0 for *AtTAS1c-ABCBs* transformation. *Arabidopsis* seeds were surface sterilized by chlorine gas, seeds were then sown in Petri dishes (12 cm × 12 cm) containing sterile half-strength Murashige and Skoog medium (0.5 × MS salts, 0.8% sucrose, 0.5 g/l 2-(N-morpholino) ethanesulfonic acid, pH 5.7, and 0.8% w/v agar), and grown under continuous light, after 3 days vernalization at 4°C.

Plasmid construction

Most constructs were generated by the Gateway system[®] (Invitrogen, Carlsbad, CA, USA). To construct the YFP fusion, coding sequences amplified from genomic DNA were cloned into pDONR-P2R-P3 (ThermoFisher Scientific) using the primers listed in Appendix Table S1. The *pro35S*-driven N-terminal YFP fusion expression clones were constructed by recombining pEN-L4-35S-R1 (Karimi et al, 2007), pEN-L1-Y-L2 (Karimi et al, 2007) and the respective CDS clones into pH7m34GW using multisite LR recombination. For the *promoter:NLS-GFP-GUS* reporters, ~2 kb promoter fragments upstream of the coding sequence were amplified from genomic DNA using primers listed in Appendix Table S1 and subsequently cloned into pENTR[™] TOPO[®] vector (pENTR[™]/D-TOPO[®] Cloning Kits, ThermoFisher Scientific) to generate the corresponding entry clones. The *promoter:NLS-GFP-GUS* was generated by performing an LR recombination reaction between Nuclear GFP fusion (pEN-L1-NF-L2) (Karimi et al, 2007), GUS reporter (pEN-R2-S*-L3) (Karimi et al, 2007) and pH7m34GW (Karimi et al, 2007). *syn-tasi-1522A* and *B* constructs were generated using primers TASI-IIIa/b-F/R (Appendix Table S1) as described (Carbonell et al, 2014; Fahlgren et al, 2016) and were recombined to pH7m24GW together with pEN-L4-pPIN2-R1 (Marques-Bueno et al, 2016).

The *pWOX5:XVE>>YUC1-2A-TAA1* construct was generated by cloning the *YUC1-2A-TAA1* cassette into XhoI and SpeI sites of the pER8 vector (Zuo et al, 2000). The full-length cDNA of *YUC1* was cloned into the BamHI site and the full-length cDNA of *TAA1* into the BglII site of the pM2A vector containing 2A peptides (Kim et al, 2011). For QC-specific activation of the *YUC1-2A-TAA1* cassette, the genomic DNA of *WOX5* promoter (*WOX5pF*: CAATATATCCTGTCAAACaaagactttatctaccaactca; *WOX5pR*: GCCGTTAACGCTTTCATcgcttcagatgtaaagctcctcaactgt) was used.

Design of amiRNA and syn-tasiRNA sequences

amiRNA and syn-tasiRNA sequences were designed using the online tools P-SAMS amiRNA Designer and P-SAMS syn-tasiRNA Designer (Fahlgren et al, 2016). For most constructs, no specificity filtering could be applied. To identify putative predicted off-targets, we used the Web MicroRNA Designer Target Search tool (<http://wmd3.weigelworld.org/>) (Ossowski et al, 2008). The following (standard) settings were used: genome (Araport11 201606 cDNA), mismatches 5, apply miRNA filter (yes), Perfect-match dG Cut-off (70), Hybridization temperature (23), Folding program (RNAfold),

Show flanking sequence (no), show only one isoform (yes), sort mode (ascending order).

Generation of *pWOX5:XVE>>YUC1-TAA1* lines

pWOX5:XVE>>YUC1-2A-TAA1 (*pWOX5>>YUC1-TAA1*) was introduced into the *DR5:VENUS* background by transformation and 10 independent lines were selected. Homozygous lines for both *pWOX5>>YUC1-TAA1* and *DR5:VENUS* were crossed to *amiR-2572* lines to generate F1 seeds. Homozygous plants for *pWOX5>>YUC1-TAA1*, *DR5:VENUS* and *amiR-2572* were gained by resistance selection and phenotyping in the F3 population.

Agrobacterium and *Arabidopsis* transformation

Agrobacterium tumefaciens strain GV3101 was transformed with the relevant binary plasmids via the freeze–thaw procedure (Chen et al, 1994). An individual PCR confirmed *Agrobacterium* colony was used for floral dip (Clough & Bent, 1998). Transformants were selected, and the segregation of the T2 was analyzed using appropriate antibiotics.

Phenotyping and LR staging

To quantify the LR phenotype in wild-type plants and mutants, emerged LR of whole seedlings were counted under a dissecting microscope, 8 days after germination. Root lengths were measured via Fiji (ImageJ 1.52n) (Schindelin et al, 2015) using digital images obtained by scanning the Petri dishes. To analyze the LR primordial stages, root samples were cleared as described previously (Malamy & Benfey, 1997). All samples were analyzed by differential interference contrast microscopy (Olympus BX51).

Oscillation analysis and prebranch site

The Luciferase imaging of whole seedlings and oscillation expression analysis was performed as described (Xuan et al, 2018). A Lumazon FA imaging system (Nippon Roper) carrying a CCD camera from Princeton Instruments Ltd. (Trenton, NJ, USA) or NightSHADE LB985 *in vivo* plant imaging system (BERTHOLD TECHNOLOGIES) carrying a deep-cooled slow scan CCD camera from Andor Instruments Ltd. (Belfast, UK) were used for luciferase imaging.

To monitor the pre-branch site numbers, we used 8-day-old *DR5:LUC* seedlings for pre-branch site quantification. The D-luciferin solution (1 mM) was sprayed gently on the seedlings, kept for 10 min in the dark and imaged in the Lumazon system with a 15-min exposure time. Static luminescence signals that were visible along the primary root outside the OZ were counted as pre-branch sites.

To monitor the periodic time and amplitude of DR5 oscillations. Three-day-old *DR5:LUC* seedlings were transferred to plate spraying with 1 mM D-luciferin solution. The sequential images of the root tip are taken every 15 min with 7 min exposure time. The luciferase signal was quantified by measuring the analog digital units per pixel with the Fiji software. A square region was selected where a pre-branch site is formed, and this region should cover DR5 oscillation that occurred prior to pre-branch site formation. The signal intensity

changes in this region overall images of the movie were measured (Appendix Fig S7B and C). The difference between the highest value and lowest value of *DR5:LUC* in the OZ defines the amplitude of DR5 oscillations (Appendix Fig S7C). The period of the DR5 oscillations was determined based on the number of frames that space a *DR5:LUC* maximum in the OZ (Xuan et al, 2018).

Macroview stereo microscope

To monitor the *DR5:VENUS* signal over time, an Olympus MVX10 macroview stereo microscope was applied to image the fluorescence signal from vertical growing *Arabidopsis* roots as described (Xuan et al, 2016). Three-day-old seedlings were imaged every 10 min with 1 s exposure time to visualize the *DR5:VENUS* stripes. To determine the time between the consecutive disappearances of the nuclear-localized fluorescence signals in the most distal lateral root cap cell files. The time-lapse pictures were saved as tiff files and further analyzed with FIJI software. The number of frames up to the frame with a complete absence of the fluorescence signal in the most distal lateral root cap, were counted. The time between two consecutive events was calculated based on the number of frames counted.

Confocal microscopy

For reporter lines and translational fusion, seedlings were imaged on a Zeiss 710 confocal microscope. For the propidium iodide (PI)-treated root images, seedlings were stained with 2 µg/ml PI for 3 min, washed with water, and used for confocal imaging. For root imaging, GFP was excited at 488 nm and acquired at 500–530 nm. YFP was excited at 514 and the emission between 519–564 nm was collected for YFP and between 614–735 nm for PI. Confocal settings were kept constant between WT (Col-0), *syn-tasi-1522A#1* and *amiR-2572* F1 progeny with either *pro35S:YFP-ABC15*, *B16*, *B17*, *B18*, and *B22*. Fluorescence intensities were measured by FIJI software (<https://imagej.net/Fiji>). The average intensity was measured in a fixed-size dashed line box for all seedlings by the “rectangle tool”.

For the *pWOX5:XVE>>YUC1-2A-TAA1* experiments seeds were sown on MS plates, stratified at 4°C for 2 days, and grown vertically in the growth chamber for 4 days at 21°C. Four-day-old seedlings of the *pWOX5:XVE>>YUC1-2A-TAA1*, *DR5:VENUS* in Col-0 and *amiR-2572* background were treated with 5 µM estradiol for the indicated time-points. Seedlings were stained in 10 mg/l propidium iodide for 2 min and rinsed in water for 30 s. Confocal microscopy was performed using a Zeiss LSM780 inverted confocal microscope equipped with a 20×/0.8 M27 objective lens. VENUS and propidium iodide were excited using an argon-ion laser and a diode laser, respectively. VENUS was excited at 514 nm and detected at 518–588 nm, and propidium iodide was excited at 561 nm and detected at 588–718 nm.

GUS staining and root sectioning

The GUS assay was performed as previously described (Beeckman & Viane, 2000). For *Arabidopsis* cross-section root specimens, GUS-stained seedlings were subjected to fixation, dehydration, and embedding as previously described (De Smet et al, 2004). GUS-

stained tissues were imaged using a Leica Bino, Olympus BX51 microscope, and a Keyence VHX-7000 microscope.

Genotyping

T-DNA lines for the ABCB single mutants were ordered from The *Arabidopsis* Information Resource (<https://www.arabidopsis.org/>), and genotyping primers for T-DNA insertion were designed using the T-DNA Primer Design Tool powered by Genome Express Browser Server (GEBD) (<http://signal.salk.edu/tdnaprimers.2.html>). Homozygous mutants were selected by PCR performed with primers listed in Appendix Table S1.

RNA extraction and RT-Q-PCR

Total RNA was extracted with the ReliaPrep™ RNA tissue Miniprep System (Promega) from plants grown *in vitro*. cDNA synthesis was performed with a random and Oligo-d(T) primer mix (Quanta qScript cDNA SuperMix). RT-qPCR was done on a LightCycler 480 (Roche Diagnostics) on 384-well plates with LightCycler 480 SYBR Green I Master (Roche). qPCR data were processed and analyzed with qbase⁺ software. qPCR was performed with primers listed in Appendix Table S1.

Auxin transport measurements

Simultaneous ³H-IAA and ¹⁴C-benzoic acid (BA) and other hormones exported from tobacco (*N. benthamiana*) and *Arabidopsis* mesophyll protoplasts were analyzed as described (Henrichs et al, 2012). Tobacco mesophyll protoplasts were prepared 4 days after Agrobacterium-mediated transfection with *pro35S:ABCB1-YFP*, *pro35S:YFP-ABCB15*, *pro35S:YFP-ABCB16*, *pro35S:YFP-ABCB17*, *pro35S:YFP-ABCB18*, *pro35S:YFP-ABCB22*, and mutation. Relative export from protoplasts is calculated from exported radioactivity into the supernatant as follows: (radioactivity in the supernatant at time $t = 10$ min) – (radioactivity in the supernatant at time $t = 0$) × (100%)/(radioactivity in the supernatant at $t = 0$ min); presented are mean values from > 4 independent transfections or protoplast preparations. Shootward (basipetal) polar auxin transport (PAT) in roots was measured as described (Lewis & Muday, 2009).

For validating the integrity of exported IAA, [2,4,5,6,7-²H₅]IAA (D5-IAA) was used in vector control tobacco export experiments as described above. Export supernatants were acidified using formic acid to pH < 3 and desalted on self-packed C₁₈-SPE columns. After elution with 0.1% formic acid in acetonitrile, samples were dried and resuspended in HPLC mobile phase. LC-MS measurements were performed on a QExactive Plus mass spectrometer (Thermo Fisher) coupled to an EasyLC 1000 nanoflow-HPLC. The mass spectrometer was operated in positive ion mode (ESI) with an electron spray voltage of 2.3 kV at 250°C of the heated capillary temperature. Fragmentation was induced by a normalized collision energy of 30%.

CRISPR/Cas9 mutagenesis and selection of mutant alleles

All single-guide (sg) RNAs in this study were designed using the CRISPR-P tool (<http://cbi.hzau.edu.cn/cgi-bin/CRISPR>) (Lei et al, 2014) to align the ABCBs coding sequence. The sgRNAs were designed to

target multiple ABCBs at once: sgRNA-19 targets ABCB16, 18, 22, 17 (20% cleavage), and 15 (0.3% cleavage); sgRNA-5 targets ABCB16, 17, 18 and 22 (61% cleavage); sgRNA-20 targets ABCB18, 22, 16 (92% cleavage), 17 (10% cleavage) and 15 (0.1% cleavage); sgRNA3 targets ABCB16, 18, 17 (0.4% cleavage), and 15 (0.1% cleavage) and sgRNA4 targets ABCB16, 17, 18 (49% cleavage), and 15 (0.1% cleavage). Vectors were assembled using the Golden Gate cloning system (Engler et al, 2014). To generate the CRISPR_A construct, the sgRNA-19, sgRNA-20, sgRNA-3 and sgRNA-4 were cloned downstream of the *Arabidopsis* U6 promoter (pATU6) in the Level 1 acceptors pICH47761, pICH47772, pICH47781 and pICH47791, respectively, as previously described (Soyk et al, 2017). In the CRISPR_B construct, the sgRNA-19, sgRNA-5, and sgRNA-20 were cloned into L1 acceptors pICH47761, pICH47772, and pICH47781, respectively, following the above procedure. The Level 1 constructs were assembled in the binary Level 2 vector pAGM4723. sgRNA sequences and primers used for genotyping are listed in Appendix Table S1.

For the CRISPR_C construct, the 20 nt protospacer (ACAT-TAGTCCAGGGATCAAG) was picked to target ABCB16 and 18. The oligos (FW: attGACATTAGTCCAGGGATCAAG; REV: aaacCTTGATCCCTGGACTAATGT) were annealed and cloned into a modified binary vector pDe-CAS9-Crimera which contains a PPT cassette and two BsaI sites. In brief, the oligos were incubated at 95°C for 5 min and cooled at RT for 20 min. The annealed oligos and the pDe-CAS9-Chimera vector were added in the following reaction (20 µl): 3 µl of annealed oligos; ~150 ng of CAS9 vector; 1 µl T4 ligase (400,000 units/ml, NEB); 1 µl BsaI-HF v2 (20,000 units/ml, NEB); Cutsmart buffer (NEB) and T4 ligase buffer (NEB). The thermal cycler conditions were 37°C for 5 min followed by 16°C for 5 min for 35 cycles, 50°C for 20 min and 80°C for 20 min. 1/10 of the reaction was transformed into *E. coli* DH5α.

Box plots

Box plots were generated by a web tool BoxPlotR (<http://shiny.chemgrid.org/boxplotr/>) (Spitzer et al, 2014), center lines show the medians; box limits indicate the 25th and 75th percentiles as determined by R software; whiskers extend 1.5 times the interquartile range from the 25th and 75th percentiles, outliers are represented by dots.

Experimental study design and statistics

No statistical methods were used to estimate the sample size. No blinding was done.

Data availability

This study includes no data deposited in external repositories.

Expanded View for this article is available [online](#).

Acknowledgements

We thank Jose Alonso and Thomas Jacobs for providing early access to unpublished materials at the beginning of this project and Michael Stumpe (Metabonomics and Proteomics Platform UNIFR) for conducting IAA analyses. This work was supported by grants from the Swiss National Funds (31003A-165877/1) to

MG, the China Scholarship Council to JC, PH and JX, the European Research Council Starting Grant (757683-RobustHormoneTrans) to ES, the PBC postdoc fellowship to YH and YZ, and FWO research grant (G002220N) to SV.

Author contributions

Jian Chen: Conceptualization; formal analysis; investigation; visualization; writing – original draft; writing – review and editing. **Yangjie Hu:** Conceptualization; formal analysis; investigation; visualization; writing – original draft; writing – review and editing. **Pengchao Hao:** Formal analysis; investigation. **Tashi Tsering:** Formal analysis; investigation. **Jian Xia:** Formal analysis; investigation. **Yuqin Zhang:** Resources. **Ohad Roth:** Resources. **Maria F Njo:** Investigation. **Lieven Sterck:** Formal analysis. **Yun Hu:** Resources. **Yunde Zhao:** Supervision. **Danny Geelen:** Supervision. **Markus Geisler:** Conceptualization; formal analysis; supervision; funding acquisition; writing – original draft; writing – review and editing. **Eilon Shani:** Conceptualization; supervision; funding acquisition; writing – original draft; writing – review and editing. **Tom Beeckman:** Conceptualization; supervision; funding acquisition; writing – original draft; writing – review and editing. **Steffen Vanneste:** Conceptualization; supervision; funding acquisition; writing – original draft; writing – review and editing.

Disclosure and competing interests statement

The authors declare that they have no conflict of interest.

References

- Adamowski M, Friml J (2015) PIN-dependent auxin transport: action, regulation, and evolution. *Plant Cell* 27: 20–32
- Bandyopadhyay A, Blakeslee JJ, Lee OR, Mravec J, Sauer M, Titapiwatanakun B, Makam SN, Bouchard R, Geisler M, Martinoia E *et al* (2007) Interactions of PIN and PGP auxin transport mechanisms. *Biochem Soc Trans* 35: 137–141
- Beeckman T, Viane R (2000) Embedding thin plant specimens for oriented sectioning. *Biotech Histochem* 75: 23–26
- Blakeslee JJ, Bandyopadhyay A, Lee OR, Mravec J, Titapiwatanakun B, Sauer M, Makam SN, Cheng Y, Bouchard R, Adamec J *et al* (2007) Interactions among PIN-FORMED and P-glycoprotein auxin transporters in *Arabidopsis*. *Plant Cell* 19: 131–147
- Bustillo-Avendano E, Serrano-Ron L, Moreno-Risueno MA (2022) The root clock as a signal integrator system: ensuring balance for survival. *Front Plant Sci* 13: 886700
- Carbonell A, Takeda A, Fahlgren N, Johnson SC, Cuperus JT, Carrington JC (2014) New generation of artificial MicroRNA and synthetic trans-acting small interfering RNA vectors for efficient gene silencing in *Arabidopsis*. *Plant Physiol* 165: 15–29
- Chen H, Nelson RS, Sherwood JL (1994) Enhanced recovery of transformants of *Agrobacterium tumefaciens* after freeze-thaw transformation and drug selection. *Biotechniques* 16: 670
- Clough SJ, Bent AF (1998) Floral dip: a simplified method for agrobacterium-mediated transformation of *Arabidopsis thaliana*. *Plant J* 16: 735–743
- De Rybel B, Vassileva V, Parizot B, Demeulenaere M, Grunewald W, Audenaert D, Van Campenhout J, Overvoorde P, Jansen L, Vanneste S *et al* (2010) A novel aux/IAA28 signaling cascade activates GATA23-dependent specification of lateral root founder cell identity. *Curr Biol* 20: 1697–1706
- De Rybel B, Audenaert D, Xuan W, Overvoorde P, Strader LC, Kepinski S, Hoye R, Brisbois R, Parizot B, Vanneste S *et al* (2012) A role for the root cap in root branching revealed by the non-auxin probe naxillin. *Nat Chem Biol* 8: 798–805
- De Smet I, Chaerle P, Vanneste S, De Rycke R, Inze D, Beeckman T (2004) An easy and versatile embedding method for transverse sections. *J Microsc* 213: 76–80
- De Smet I, Tetsumura T, De Rybel B, Frei dit Frey N, Laplaze L, Casimiro I, Swarup R, Naudts M, Vanneste S, Audenaert D *et al* (2007) Auxin-dependent regulation of lateral root positioning in the basal meristem of *Arabidopsis*. *Development* 134: 681–690
- Deslauriers SD, Spalding EP (2021) Electrophysiological study of *Arabidopsis* ABCB4 and PIN2 auxin transporters: evidence of auxin activation and interaction enhancing auxin selectivity. *Plant Direct* 5: e361
- Dubrovsky JG, Sauer M, Napsucially-Mendivil S, Ivanchenko MG, Friml J, Shishkova S, Celenza J, Benkova E (2008) Auxin acts as a local morphogenetic trigger to specify lateral root founder cells. *Proc Natl Acad Sci USA* 105: 8790–8794
- Engler C, Youles M, Gruetzner R, Ehnert TM, Werner S, Jones JD, Patron NJ, Marillonnet S (2014) A golden gate modular cloning toolbox for plants. *ACS Synth Biol* 3: 839–843
- Fahlgren N, Hill ST, Carrington JC, Carbonell A (2016) P-SAMS: a web site for plant artificial microRNA and synthetic trans-acting small interfering RNA design. *Bioinformatics* 32: 157–158
- Geisler M, Kolukisaoglu HU, Bouchard R, Billion K, Berger J, Saal B, Frangne N, Koncz-Kalman Z, Koncz C, Dudler R *et al* (2003) TWISTED DWARF1, a unique plasma membrane-anchored immunophilin-like protein, interacts with *Arabidopsis* multidrug resistance-like transporters AtPGP1 and AtPGP19. *Mol Biol Cell* 14: 4238–4249
- Geisler M, Blakeslee JJ, Bouchard R, Lee OR, Vincenzetti V, Bandyopadhyay A, Titapiwatanakun B, Peer WA, Bailly A, Richards EL *et al* (2005) Cellular efflux of auxin catalyzed by the *Arabidopsis* MDR/PGP transporter AtPGP1. *Plant J* 44: 179–194
- Geisler M, Aryal B, di Donato M, Hao P (2017) A critical view on ABC transporters and their interacting partners in auxin transport. *Plant Cell Physiol* 58: 1601–1614
- Grieneisen VA, Xu J, Maree AF, Hogeweg P, Scheres B (2007) Auxin transport is sufficient to generate a maximum and gradient guiding root growth. *Nature* 449: 1008–1013
- Hao P, Xia J, Liu J, diDonato M, Pakula K, Bailly A, Jasinski J, Geisler M (2020) A conserved D/E-P motif in the nucleotide binding domain of plant ABCB/PGP-type ABC transporters defines their auxin transport capacity. *J Biol Chem* 295: 13094–13105
- Heisler MG, Ohno C, Das P, Sieber P, Reddy GV, Long JA, Meyerowitz EM (2005) Patterns of auxin transport and gene expression during primordium development revealed by live imaging of the *Arabidopsis* inflorescence meristem. *Curr Biol* 15: 1899–1911
- Henrichs S, Wang B, Fukao Y, Zhu J, Charrier L, Bailly A, Oehring SC, Linnert M, Weiwad M, Ender A *et al* (2012) Regulation of ABCB1/PGP1-catalysed auxin transport by linker phosphorylation. *EMBO J* 31: 2965–2980
- Hu Y, Omary M, Hu Y, Doron O, Hoermayer L, Chen Q, Megides O, Chekli O, Ding Z, Friml J *et al* (2021) Cell kinetics of auxin transport and activity in *Arabidopsis* root growth and skewing. *Nat Commun* 12: 1657
- Ito H, Gray WM (2006) A gain-of-function mutation in the *Arabidopsis* pleiotropic drug resistance transporter PDR9 confers resistance to auxinic herbicides. *Plant Physiol* 142: 63–74
- Jenness MK, Tayengwa R, Bate GA, Tapken W, Zhang Y, Pang C, Murphy AS (2022) Loss of multiple ABCB auxin transporters recapitulates the major twisted dwarf 1 phenotypes in *Arabidopsis thaliana*. *Front Plant Sci* 13: 840260

- Kaneda M, Schuetz M, Lin BS, Chanis C, Hamberger B, Western TL, Ehrling J, Samuels AL (2011) ABC transporters coordinately expressed during lignification of *Arabidopsis* stems include a set of ABCBs associated with auxin transport. *J Exp Bot* 62: 2063–2077
- Kang J, Park J, Choi H, Burla B, Kretschmar T, Lee Y, Martinoia E (2011) Plant ABC transporters. *Arabidopsis Book* 9: e0153
- Kang J, Yim S, Choi H, Kim A, Lee KP, Lopez-Molina L, Martinoia E, Lee Y (2015) Abscisic acid transporters cooperate to control seed germination. *Nat Commun* 6: 8113
- Karimi M, Bleys A, Vanderhaeghen R, Hilson P (2007) Building blocks for plant gene assembly. *Plant Physiol* 145: 1183–1191
- Kim JH, Lee SR, Li LH, Park HJ, Park JH, Lee KY, Kim MK, Shin BA, Choi SY (2011) High cleavage efficiency of a 2A peptide derived from porcine teschovirus-1 in human cell lines, zebrafish and mice. *PLoS One* 6: e18556
- Kubeš M, Yang H, Richter GL, Cheng Y, Młodzieńska E, Wang X, Blakeslee JJ, Carraro N, Petrásek J, Žažimalová E et al (2012) The *Arabidopsis* concentration-dependent influx/efflux transporter ABCB4 regulates cellular auxin levels in the root epidermis. *Plant J* 69: 640–654
- Lee M, Choi Y, Burla B, Kim YY, Jeon B, Maeshima M, Yoo JY, Martinoia E, Lee Y (2008) The ABC transporter AtABC14 is a malate importer and modulates stomatal response to CO₂. *Nat Cell Biol* 10: 1217–1223
- Lei Y, Lu L, Liu HY, Li S, Xing F, Chen LL (2014) CRISPR-P: a web tool for synthetic single-guide RNA design of CRISPR-system in plants. *Mol Plant* 7: 1494–1496
- Lewis DR, Muday GK (2009) Measurement of auxin transport in *Arabidopsis thaliana*. *Nat Protoc* 4: 437–451
- Lewis DR, Miller ND, Splitt BL, Wu G, Spalding EP (2007) Separating the roles of acropetal and basipetal auxin transport on gravitropism with mutations in two *Arabidopsis* multidrug resistance-like ABC transporter genes. *Plant Cell* 19: 1838–1850
- Malamy JE, Benfey PN (1997) Organization and cell differentiation in lateral roots of *Arabidopsis thaliana*. *Development* 124: 33–44
- Marques-Bueno MDM, Morao AK, Cayrel A, Platre MP, Barberon M, Caillieux E, Colot V, Jaillais Y, Roudier F, Vert G (2016) A versatile multisite gateway-compatible promoter and transgenic line collection for cell type-specific functional genomics in *Arabidopsis*. *Plant J* 85: 320–333
- Mashiguchi K, Tanaka K, Sakai T, Sugawara S, Kawaide H, Natsume M, Hanada A, Yaeno T, Shirasu K, Yao H et al (2011) The main auxin biosynthesis pathway in *Arabidopsis*. *Proc Natl Acad Sci USA* 108: 18512–18517
- Mellor NL, Voss U, Janes G, Bennett MJ, Wells DM, Band LR (2020) Auxin fluxes through plasmodesmata modify root-tip auxin distribution. *Development* 147: dev181669
- Mellor NL, Voss U, Ware A, Janes G, Barrack D, Bishopp A, Bennett MJ, Geisler M, Wells DM, Band LR (2022) Systems approaches reveal that ABCB and PIN proteins mediate co-dependent auxin efflux. *Plant Cell* 34: 2309–2327
- Moreno-Risueno MA, Van Norman JM, Moreno A, Zhang J, Ahnert SE, Benfey PN (2010) Oscillating gene expression determines competence for periodic *Arabidopsis* root branching. *Science* 329: 1306–1311
- Motte H, Vanneste S, Beeckman T (2019) Molecular and environmental regulation of root development. *Annu Rev Plant Biol* 70: 465–488
- Mravec J, Kubes M, Bielach A, Gaykova V, Petrásek J, Skupa P, Chand S, Benkova E, Žažimalová E, Friml J (2008) Interaction of PIN and PGP transport mechanisms in auxin distribution-dependent development. *Development* 135: 3345–3354
- Ossowski S, Schwab R, Weigel D (2008) Gene silencing in plants using artificial microRNAs and other small RNAs. *Plant J* 53: 674–690
- Rosquete MR, Barbez E, Kleine-Vehn J (2012) Cellular auxin homeostasis: gatekeeping is housekeeping. *Mol Plant* 5: 772–786
- Ruzicka K, Strader LC, Bailly A, Yang H, Blakeslee J, Langowski L, Nejedla E, Fujita H, Itoh H, Syono K et al (2010) *Arabidopsis* PIS1 encodes the ABCG37 transporter of auxinic compounds including the auxin precursor indole-3-butyric acid. *Proc Natl Acad Sci USA* 107: 10749–10753
- Santelia D, Vincenzetti V, Azzarello E, Bovet L, Fukao Y, Duchting P, Mancuso S, Martinoia E, Geisler M (2005) MDR-like ABC transporter AtPGP4 is involved in auxin-mediated lateral root and root hair development. *FEBS Lett* 579: 5399–5406
- Schindelin J, Rueden CT, Hiner MC, Eliceiri KW (2015) The ImageJ ecosystem: an open platform for biomedical image analysis. *Mol Reprod Dev* 82: 518–529
- Soyk S, Lemmon ZH, Oved M, Fisher J, Liberatore KL, Park SJ, Goren A, Jiang K, Ramos A, van der Knaap E et al (2017) Bypassing negative epistasis on yield in tomato imposed by a domestication gene. *Cell* 169: 1142–1155
- Spitzer M, Wildenhain J, Rappsilber J, Tyers M (2014) BoxPlotR: a web tool for generation of box plots. *Nat Methods* 11: 121–122
- Stoeckle D, Thellmann M, Vermeer JE (2018) Breakout-lateral root emergence in *Arabidopsis thaliana*. *Curr Opin Plant Biol* 41: 67–72
- Swarup R, Bhosale R (2019) Developmental roles of AUX1/LAX auxin influx carriers in plants. *Front Plant Sci* 10: 1306
- Terasaka K, Blakeslee JJ, Titapiwatanakun B, Peer WA, Bandyopadhyay A, Makam SN, Lee OR, Richards EL, Murphy AS, Sato F et al (2005) PGP4, an ATP binding cassette P-glycoprotein, catalyzes auxin transport in *Arabidopsis thaliana* roots. *Plant Cell* 17: 2922–2939
- Ung KL, Winkler M, Schulz L, Kolb M, Janacek DP, Dedic E, Stokes DL, Hammes UZ, Pedersen BP (2022) Structures and mechanism of the plant PIN-FORMED auxin transporter. *Nature* 609: 605–610
- van den Berg T, Yalamançhili K, de Garnier H, Santos Teixeira J, Beeckman T, Scheres B, Willemsen V, Ten Tusscher K (2021) A reflux-and-growth mechanism explains oscillatory patterning of lateral root branching sites. *Dev Cell* 56: 2176–2191
- Vanneste S, Friml J (2009) Auxin: a trigger for change in plant development. *Cell* 136: 1005–1016
- Won C, Shen X, Mashiguchi K, Zheng Z, Dai X, Cheng Y, Kasahara H, Kamiya Y, Chory J, Zhao Y (2011) Conversion of tryptophan to indole-3-acetic acid by tryptophan aminotransferases of *Arabidopsis* and *Yuccas* in *Arabidopsis*. *Proc Natl Acad Sci USA* 108: 18518–18523
- Wu G, Otegui MS, Spalding EP (2010) The ER-localized TWD1 immunophilin is necessary for localization of multidrug resistance-like proteins required for polar auxin transport in *Arabidopsis* roots. *Plant Cell* 22: 3295–3304
- Xuan W, Audenaert D, Parizot B, Moller BK, Njo MF, De Rybel B, De Rop G, Van Isterdael G, Mahonen AP, Vanneste S et al (2015) Root cap-derived auxin pre-patterns the longitudinal axis of the *Arabidopsis* root. *Curr Biol* 25: 1381–1388
- Xuan W, Band LR, Kumpf RP, Van Damme D, Parizot B, De Rop G, Opendacker D, Moller BK, Skorzinski N, Njo MF et al (2016) Cyclic programmed cell death stimulates hormone signaling and root development in *Arabidopsis*. *Science* 351: 384–387
- Xuan W, Opendacker D, Vanneste S, Beeckman T (2018) Long-term *in vivo* imaging of luciferase-based reporter gene expression in *Arabidopsis* roots. *Methods Mol Biol* 1761: 177–190
- Yang Z, Xia J, Hong J, Zhang C, Wei H, Ying W, Sun C, Sun L, Mao Y, Gao Y et al (2022) Structural insights into auxin recognition and efflux by *Arabidopsis* PIN1. *Nature* 609: 611–615

Zhang K, Novak O, Wei Z, Gou M, Zhang X, Yu Y, Yang H, Cai Y, Strnad M, Liu CJ (2014) *Arabidopsis* ABCG14 protein controls the acropetal translocation of root-synthesized cytokinins. *Nat Commun* 5: 3274

Zhang Y, Nasser V, Pisanty O, Omary M, Wulff N, Di Donato M, Tal I, Hauser F, Hao P, Roth O et al (2018) A transcriptome-scale amiRNA-based screen

identifies redundant roles of *Arabidopsis* ABCB6 and ABCB20 in auxin transport. *Nat Commun* 9: 4204

Zuo J, Niu QW, Chua NH (2000) Technical advance: an estrogen receptor-based transactivator XVE mediates highly inducible gene expression in transgenic plants. *Plant J* 24: 265–273